Journal of Wind Engineering & Industrial Aerodynamics 165 (2017) 46–57

Contents lists available at ScienceDirect

Journal of Wind Engineering and Industrial Aerodynamics

journal homepage: www.elsevier.com/locate/jweia

The performance of different turbulence models (URANS, SAS and DES) for predicting high-speed train slipstream

Shibo Wang[a,*], James R. Bell[a], David Burton[a], Astrid H. Herbst[b], John Sheridan[a], Mark C. Thompson[a]

[a] Fluids Laboratory for Aeronautical and Industrial Research (FLAIR), Department of Mechanical Engineering, Monash University, Australia
[b] Centre of Competence for Aero- and Thermodynamics, Bombardier Transportation, Västeras, Sweden

ARTICLE INFO

Keywords:
High-speed trains
Train aerodynamics
Slipstream
Computational Fluid Dynamics (CFD)
Unsteady Reynolds-Averaged Navier–Stokes equations (URANS)
Scale-Adaptive Simulation (SAS)
Detached Eddy Simulation (DES)

ABSTRACT

The air movement induced by a high-speed train (HST) as it passes, the slipstream, is a safety hazard to commuters and trackside workers, and can cause damage to infrastructure along track lines. Because of its importance, many numerical studies have been undertaken to investigate this phenomenon. However, to the authors' knowledge, a systematic comparison of the accuracy of different turbulence models applied to the prediction of slipstream has not yet been conducted. This study investigates and evaluates the performance of three widely used turbulence models: URANS, SAS and DES, to predict the slipstream of a full-featured generic train model, and the results are compared with wind-tunnel experimental data to determine the fidelity of the models. Specifically, this research aims to determine the suitability of different turbulence modelling approaches, involving significantly different computational resources, for modelling different aspects of slipstream.

1. Introduction

Slipstream depends on the air movement induced by a high-speed train (HST) as it passes. It is defined through the resultant induced horizontal velocity at a specific point from the train vertical centre-plane, measured in the stationary reference frame. Train slipstream can be a safety hazard to commuters and trackside workers, and can also cause damage to infrastructure along track lines. Because of these dangers, many countries have enforced regulations to limit the maximum permissible slipstream velocity, for example, countries in Europe through the European Standards (European Union Agency for Railways, 2014; Railway Applications, 2013). Therefore, minimising slipstream is one of the preliminary goals for HST development, as it poses a constraint on the design, especially if the HST is to operate at high speed. As the induced slipstream velocity depends on the flow development around a HST, an accurate prediction of the flow structure is essential to understanding the slipstream velocity.

Compared with conventional road vehicles, HSTs have a more streamlined shape with no fixed flow separation points, a much larger length-to-width ratio, and they travel significantly faster. Therefore, the flow around a HST is unique, and existing knowledge of neither conventional road vehicles aerodynamics nor aircraft aerodynamics can be directly utilised to understand HST aerodynamics. Consequently, much effort has been channelled towards studying HST slipstream numerically.

For high Reynolds number flows, as the range for time and length scales that describe the flow depends on the Reynolds number, some level of turbulence modelling is required. Much effort has been directed towards improving the accuracy and efficiency of the numerical modelling for complex turbulent flows, e.g., through more adaptable meshing strategies and the development of increasingly complex turbulence models. As a HST wake is highly turbulent, three-dimensional and time-dependent, appropriate turbulence modelling is essential for accurate prediction. Currently, the most widely used time-dependent turbulence models are unsteady-RANS (Reynolds-Averaged Navier–Stokes) (URANS), SAS (Scale-Adaptive Simulation), DES (Detached Eddy Simulation) and LES (Large Eddy Simulation). Due to the high computational cost of (pure) LES at high Reynolds numbers, at this stage utilising LES to study HST aerodynamics is still prohibitive (Hemida et al., 2014; Östh et al., 2015). Therefore, this study focuses on three less expensive numerical approaches that appear more applicable to high-speed train aerodynamics research: URANS, SAS and DES.

RANS decomposes the Navier–Stokes equations by splitting the flow velocity into mean and fluctuating components, focusing on solving for the time- or ensemble-mean flow. RANS has been optimised

* Corresponding author.
E-mail address: shibo.wang@monash.edu (S. Wang).

http://dx.doi.org/10.1016/j.jweia.2017.03.001
Received 9 December 2016; Received in revised form 10 February 2017

for time- or ensemble mean predictions. By retaining the time-dependent terms, (U)RANS can be used to predict the large-scale dynamics for absolutely unstable flows. For example, Schulte-Werning et al. (2003) utilised URANS to predict the spanwise vortex shedding from the tail of a train. Paradot et al. (2002) showed that RANS can achieve a good agreement with the wind tunnel experiments on time-averaged flow topology prediction and drag estimation, while in order to achieve a quantitatively accurate prediction in the complex areas, unsteady calculations are essential. SAS modifies the classic URANS approach by incorporating the von Karman length scale. Interestingly, the modified model can capture the large temporal and spatial scales of the plain URANS approach, but by automatically adjusting the turbulent length and time scales according to the spatial and temporal resolution, it can capture increasingly finer scales (Menter and Egorov, 2010; Egorov et al., 2010). It has been used as an alternative method to study complex industrial flows due to its good balance between accuracy and cost. The fidelity of the SAS model has been verified on various engineering cases, such as bluff body aerodynamics (Egorov et al., 2010), aero-acoustics (Yang et al., 2014) and turbine machinery (Fossi et al., 2015). However, to the authors' knowledge, SAS has not yet been applied to train aerodynamics. DES blends the LES and RANS approaches, utilising RANS to approximate the mean boundary layer behaviour and applying LES to capture the time-dependent flow away from wall boundaries. Therefore, the turbulence spectrum away from boundaries can be adequately resolved. DES has been widely used to study different aspects of train aerodynamics, such as slipstream assessment (Huang et al., 2016) and underbody flows (Zhang et al., 2016). Morden et al. (2015) compared RANS and DES approaches with wind tunnel data on predicting the surface pressures upon a Class 43 High-Speed Train, and concluded that DES is superior in replicating the experimental results. Generally, a model that captures more of the full range of flow structures is more computationally demanding.

However, to the authors' knowledge, a systematic comparison of the strengths and weaknesses of different turbulence models for predicting different aspects of HST slipstream is yet to be undertaken, and this has motivated this current study.

Specifically, this study aims to investigate and evaluate the accuracy of three widely used turbulence models, URANS, SAS and DES, for predicting the flow field around a typical HST: the *ICE3* (described below). The comparison covers five aspects of HST aerodynamics: slipstream assessment, aerodynamic drag coefficient prediction, gust analysis, mean flow structure and wake dynamics. Additionally, the predictive capability of each turbulence model under two control variables, timestep and grid resolution, is investigated, as these are the two key parameters which significantly affect both the accuracy and the computational cost. Moreover, the numerical results are compared with wind tunnel experimental data to determine the fidelity of the models (Bell et al., 2014).

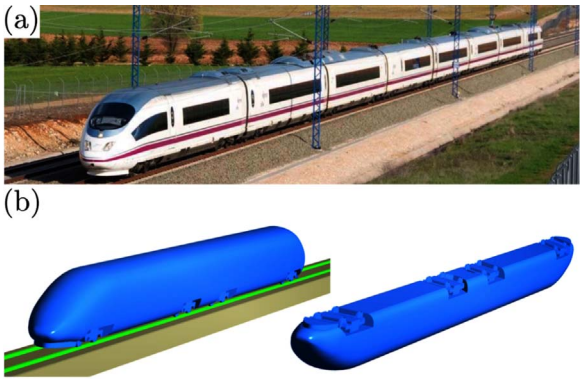

Fig. 1. Comparison between the full-scale ICE train and numerical model: (a) full-scale operational ICE3 train; (b) simplified numerical model. (Photo provided courtesy of Bombardier Transportation).

This paper is structured as follows. Initially, the numerical set-up, including defining the train geometry, the computational domain and corresponding boundary conditions, the meshing strategy, discretisation schemes, and turbulence models are introduced in the *Methodology* section. The *Results and Analysis* section consists of two sub-sections. In the first, all simulation cases are initially compared based on the slipstream velocity and the aerodynamic drag coefficient. In the second section, based on the previous comparison and typical utilisation of each turbulence model, typical cases with representative grid resolutions and timesteps are selected for a more detailed analysis. In this section, gust phenomena, time-averaged flow structure and wake dynamics are studied, and their interrelationship with the slipstream prediction is assessed. To conclude, the strengths and weaknesses of each turbulence model for predicting HST slipstream are summarised.

2. Methodology

2.1. Geometry

This study is based on a *Deutsche Bahn Inter-City-Express 3* (ICE3) high-speed train, a widely operated train in European and Asian countries, as shown in Fig. 1a. *ICE3* has a representative HST external shape, and its Computer-Aided Design (CAD) model is freely available from the DIN Standards Railway Committee (FSF) (FSF, 2014). The numerical analysis is based on a slightly geometrically simplified model, which has a length–width–height ratio of approximately 50:3:4, as illustrated in Fig. 1b. Although the train model is simplified, omitting details such as the gaps between carriages and the air-conditioning units, it still includes key geometry features that have a strong influence on the wake, in particular, the bogies and snow-plows. The train is located on a *Single Track Ballast and Rail* (STBR) ground configuration, with the dimensions specified in CEN guidelines (Railway Applications, 2013). The thickness of the rails is extended from 50 mm to the wheel width of 135 mm (in full-scale) in order to represent a realistic contact between the rails and wheels.

2.2. Domain and boundary conditions

The train is positioned in a computational domain consisting of hexahedral elements, as illustrated in Fig. 2. For the discussion, dimensions are generally normalised by the train width (W) in the spanwise direction (y-direction), or by the length (L) of the train in the streamwise direction (x-direction). The origin of the coordinate system is positioned in the spanwise mid-plane, at the height of the top surface of the rails, with x=0 corresponding to the tail tip.

A uniform velocity boundary condition with a turbulence intensity of 1% is applied at the inlet to simulate the low-turbulence horizontal-flow freestream condition in the wind tunnel. The Reynolds number (based on W) is 7.2×10^5. These values are chosen for consistency for a comparison with wind-tunnel experiments, noting that they are not representative of full-scale train operation. A zero static pressure condition is applied at the outlet boundary. A no-slip wall boundary condition is applied to all train surfaces. In order to replicate the splitter plate introduced to remove the floor boundary layer in the wind tunnel experiments (Bell et al., 2014), the floor is split into two parts, named floor 1 and floor 2. Floor 1 is 0.7L long and it employs a zero-shear wall condition. Floor 2 is 4.3L long with a no-slip wall condition. Symmetry boundary conditions are applied at the top and sides of the computational domain. Note that for a clearer visualisation of the computational setup and domain dimensions, Fig. 2 is not drawn to scale.

2.3. Meshing strategy

The general meshing strategy is based on the predominately

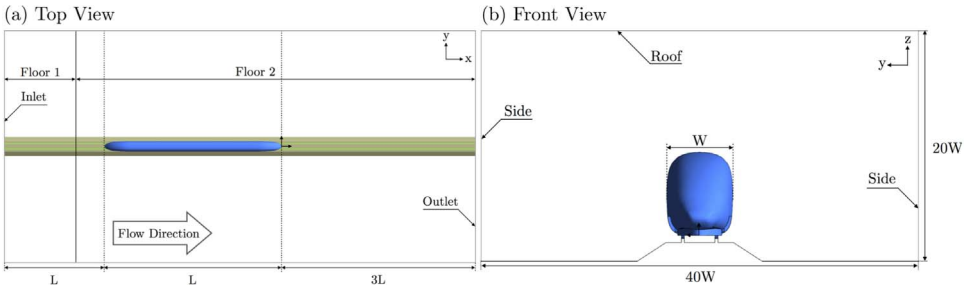

Fig. 2. Schematic of computational domain: (a) top-view; (b) front-view. (Not to scale.)

Cartesian *cut-cell* approach, allowing substantially increased mesh concentration around the train and in the wake, together with a relatively smooth transition to lower resolution away from the train. In particular, it achieves a high uniform resolution in the slipstream measurement regions, and aids in accurately capturing the boundary layers and induced flow separation from smaller-scale geometrical features. In this study, three sequentially refined grids (coarse, medium and fine grids) are constructed based on the identical meshing strategy and generally maintaining the same compression factors between meshes. Three different levels of refinement zones are utilised to achieve higher accuracy in critical regions, as illustrated in Fig. 3. *Inflation layers* are applied to all wall boundaries to capture the boundary layer development, as illustrated in Fig. 4. To ensure that all important flow features are captured, the dimensions of the refinement regions were determined based on a preliminary simulation. A smooth transition is established between the adjacent cells including between the outer inflation layer and the hexahedral grid, and at the interface of two refinement zones, as shown in Fig. 4. More details regarding the individual grid description are presented in Section 3.1.1.

2.4. Brief description of the solver

The numerical solver utilised in this research is the commercial CFD code *FLUENT*, which is part of the ANSYS 16.2 software suite. Due to the turbulent nature of slipstream, a pressure-based transient solver is used for all simulations. The *Pressure–Velocity Coupling Scheme* for RANS and SAS simulation is SIMPLEC, while the *Fractional-Step Scheme* with *Non-Iterative Time Advancement* is applied for DES, as long as the Courant number is less than unity. For spatial discretisation, the *second-order upwind scheme* is applied for all flow equations, except for SAS and DES, which utilise *bounded central differencing* for the momentum equation. The *bounded second-order implicit* formulation is applied for transient simulations for all cases. Also, for all simulations, the flow field is initialised with a second-order accuracy steady-state RANS simulation based on the Shear-Stress Transport (SST) RANS model.

Unsteady statistics are obtained by averaging the flow after it is first checked to have reached its asymptotic state. This is checked through comparisons with predictions from smaller averaging periods. A useful time scale can be constructed from the train height and freestream velocity, defining a *Reference Time Scale* ($T_{ref} = H/U_\infty$). Unsteady statistics are gathered over $195T_{ref}$, which is equivalent to three times

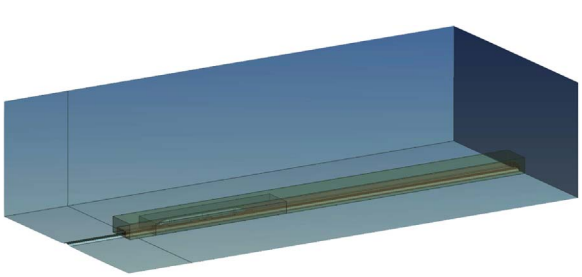

Fig. 3. The schematic of mesh refinement zones.

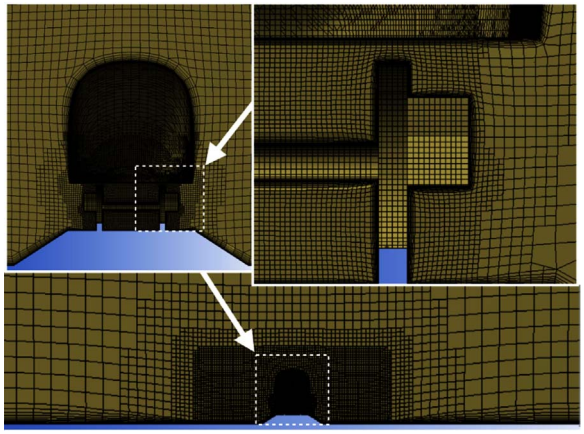

Fig. 4. A cross-section view of the mesh refinements around the train (based on the fine grid).

the time taken for the freestream flow to advect through the entire domain from inlet to outlet, or approximately 15 times the time taken for the flow to advect the length of the train.

The turbulence models are described briefly below.

2.4.1. URANS

Reynolds-averaging proceeds by first splitting the flow variables into mean and fluctuating components. Putting this decomposition into the Navier–Stokes equations and averaging gives the *Reynolds-Averaged Navier–Stokes* (RANS) equations. Keeping the time derivative of the mean velocity, which implies that the averaging procedure can be thought of as averaging over an ensemble of turbulent flow states, gives the *Unsteady* RANS (i.e., URANS) model.

The equations for the mean velocity components $\overline{u}_i$ and pressure ($\overline{p}$) are summarised as

$$\frac{\partial \overline{u}_i}{\partial x_i} = 0, \tag{1}$$

$$\frac{\partial \overline{u}_i}{\partial t} + \overline{u}_j \frac{\partial \overline{u}_i}{\partial x_j} = -\frac{1}{\rho}\frac{\partial \overline{p}}{\partial x_i} + \frac{\partial}{\partial x_j}\left(\nu \frac{\partial \overline{u}_i}{\partial x_j}\right) + \frac{1}{\rho}\frac{\partial \tau_{ij}}{\partial x_i}, \tag{2}$$

where $\tau_{ij} = \overline{u'_i u'_j}$ is the *Reynolds Stress Tensor*, which cannot formally be expressed in terms of mean flow variables; instead some level of turbulence modelling has to be applied. The usual way to proceed is to form an analogy between molecular diffusion and turbulent mixing, and thus approximate the Reynolds stress in terms of the mean flow gradient together with a spatially varying turbulent viscosity based on local turbulent time/velocity and length scales. These scales are obtained by solving two further equations, e.g., for the turbulent kinetic energy per unit mass (k) and the turbulent dissipation (ϵ) for the well-known k–ϵ model. In this study, the more sophisticated two-equation *Shear-Stress Transport* (SST) k–ω model is utilised. *Shear-Stress Transport* (SST) k–ω model is also determined as the optimal RANS model by studying a range of RANS models based on their

performances of predicting the surface pressure on a High-Speed Train (Morden et al., 2015). This blends the classical $k-\omega$ and $k-\varepsilon$ models, noting $k-\omega$ is considered a superior and better behaved model in the near-wall boundary-layer regions, and $k-\varepsilon$ is more appropriate in the outer flow. The aim is to better model flows with undefined separation points, such as exist on the smooth surfaces of a high-speed train. Of course, URANS models can only capture large-scale flow features and periodicities, such as the shedding from bluff bodies such as circular cylinders, noting that only the very large-scale vortical wake features caused by absolute instability are likely to be resolved to some level of accuracy. For a smooth geometry like a high-speed train, it is unclear how well the wake flow is likely to be captured by such a model.

2.4.2. SAS

SAS is developed from the classical URANS model, noting that the way that turbulence is incorporated is mathematically equivalent between the RANS approach and the subgrid-scale model used for *Large Eddy Simulation*. The innovation of SAS is that the von Karman length scale is introduced to capture the scale-adaptive temporal and spatial scales. This idea was initially proposed by Rotta (1972), and has been gradually improved through the years and recently integrated into the commercial CFD solver ANSYS (Menter, 2012). Unlike the URANS approach which can only capture large-scale vortex shedding, SAS is capable of resolving part of the turbulence spectrum for unstable flows depending on the spatial and temporal scales, i.e., in this case, effectively the cell size and timestep. The length scale used to construct the turbulent viscosity is given by

$$L_{vK} = \kappa \left| \frac{\overline{U}'}{\overline{U}''} \right|, \tag{3}$$

with

$$\overline{U}' = \sqrt{2 S_{ij} S_{ij}} \quad \text{and} \quad \overline{U}'' = \sqrt{\frac{\partial^2 \overline{u}_i}{\partial x_j \partial x_j} \frac{\partial^2 \overline{u}_i}{\partial x_k \partial x_k}}, \tag{4}$$

where

$$S_{ij} = \frac{1}{2}\left(\frac{\partial \overline{u}_i}{\partial x_j} + \frac{\partial \overline{u}_j}{\partial x_i} \right). \tag{5}$$

A full description of the SAS model is given in Menter and Egorov (2010) and Egorov et al. (2010).

As a scale-adaptive method, it shows a gradual transition from URANS-type to LES-type behaviour as the temporal and spatial resolution are increased. Unlike problems with LES or DES caused by insufficient grid or time resolution, SAS utilises URANS as a back-up (Menter and Egorov, 2010). A known limitation of SAS is that the scale-resolving mode is not activated unless the flow is sufficiently unstable. For this study the wake is highly turbulent, fed by flow past complex underbody structures and large-scale shedding in the wake.

2.4.3. DES

DES is a blend of RANS and LES models, utilising RANS to approximate the boundary layer and applying LES to capture the time-dependent flow away from boundaries. This study uses SST as the RANS turbulence model within the wall region. By trying not to solve the fine-scale time-dependent turbulence structures of wall boundary layers under LES, which are unlikely to strongly influence the outer flow, DES significantly reduces the computational cost of applying an LES approach to solve high Reynolds number engineering problems. To achieve this hybrid behaviour, a switch function based on the grid size is utilised to trigger the corresponding model for the respective region. The accuracy and validity of DES directly depend on accurately switching the turbulence model between the attached boundary-layer region (RANS) and free shear-flow region (LES). *Modelled-Stress Depletion* and *Grid-Induced Separation* are the two most common issues of the classical DES model (Spalart, 2009). These issues have been gradually addressed through the continuous improvements to the model. This study utilises the *Improved-Delayed-DES* (IDDES) model, which applies an improved delayed shielding function to achieve a higher accuracy within the RANS–LES blending region, which also improves the wall-modelling capability. A fuller description is given in Spalart (2009).

2.5. Wind tunnel validation case

This study has been validated against results from a wind-tunnel study based on the same simplified scale model of a high-speed train. The Reynolds number is also matched. The experiment was conducted in the Monash University 1.4 MW closed-circuit wind tunnel. A full description of the experimental set-up and results are reported in Bell et al. (2016a,b).

3. Results and analysis

To achieve the aim of systematically comparing the capability of different turbulence models for modelling HST aerodynamics, the results are presented from two perspectives. In Section 3.1, the predicted slipstream velocity profile and the aerodynamic drag coefficient of all cases are compared as a function of grid resolution and timestep. The cases run are listed in Table 1. In Section 3.2, representative cases of each model are chosen for further investigation, noting that a key selection criterion is that a URANS simulation should be significantly cheaper than SAS, which in turn should be cheaper than DES. For that study, three representative cases are studied through comparison to the wind tunnel data according to slipstream prediction, time-averaged wake structure and large-scale wake dynamics.

3.1. Overall result analysis

In this section, all cases are studied and compared based on the predictions of slipstream and aerodynamic drag. The slipstream profile is recorded 3 m (in full scale) away from the centreline of the train and at two different heights i.e., trackside height and platform height, according to the TSI specifications (European Union Agency for Railways, 2014). In this section, the comparison focuses on measurements at the trackside height (z=0.05H). Slipstream is defined as the air movement induced by a moving train, which is measured in a ground-fixed (GF) stationary reference frame, while CFD simulations are based on the train-fixed (TF) reference frame, hence a change of frame is required. The *slipstream velocity* ($U_{slipstream}$) is defined by

$$U_{slipstream} = \sqrt{(U_{GF}^2 + V_{GF}^2)}, \tag{6}$$

where

$$U_{GF} = U_\infty - U_{TF}, \quad V_{GF} = V_{TF}. \tag{7}$$

In Eqs. (6) and (7), the subscripts *GF* and *TF* indicate *ground-fixed* and *train-fixed* reference frames, respectively. Velocities, including slipstream velocities, quoted in this study are typically normalised by

Table 1
The list of all simulation cases.

Grid resolution	$0.05T_{ref}$	$0.025T_{ref}$	$0.0025T_{ref}$
Fine	URANS	URANS SAS IDDES	 SAS IDDES
Medium	URANS	SAS	IDDES
Coarse	URANS	SAS	IDDES

the freestream velocity (U_∞). Also note that slipstream is only based on the downstream (U) and transverse (V) components of the velocity. The vertical velocity component is ignored.

The comparison in this section is based on the time-averaged slipstream velocity ($\overline{U}_{slipstream}$), and its standard deviation ($\sigma_{slipstream}$). The discrepancy between the wind tunnel measurements and numerical simulations is discussed in Section 4, and potential sources of these differences are identified.

3.1.1. The influence of grid resolution

To study the effect of grid spatial resolution, in order to maintain the consistency of the comparison, the timestep for each model remains fixed with $\Delta t_{\mathrm{URANS}} = 0.05T_{ref}$, $\Delta t_{\mathrm{SAS}} = 0.025T_{ref}$ and $\Delta t_{\mathrm{IDDES}} = 0.0025T_{ref}$, reflecting the sophistication of the models and noting that the successive models progressively try to capture finer spatial and temporal scales. An underlying assumption is that only capturing the large-scale flow features can still provide reasonable predictions of slipstream and drag. This will be tested in the following sections. The reference timestep is broadly based on common practice; more details regarding timestep selection are presented in the following section on timestep selection.

Three grids with the same meshing strategy but different densities were constructed for this comparison. The overall meshing strategy is based on the Cartesian *cut-cell* meshing approach with refinements around the train and in the wake region, as introduced in the *Methodology* section. The number of cells for the coarse, medium and fine grids are approximately 3.3, 17.4, 26.6 million respectively. As the mesh gets finer, the train surface cell size and the cell size of the refinement zones are gradually decreased, and the corresponding number of inflation layers on the wall boundaries is increased. The critical meshing parameters are listed in Table 2.

The effects of grid resolution, in terms of the $\overline{U}_{slipstream}$ and $\sigma_{slipstream}$, are illustrated in Fig. 5. According to this figure, all cases show a qualitatively good agreement with the wind tunnel data. A local peak occurs near the train nose due to the head pulse, while the maximum $\overline{U}_{slipstream}$ happens at approximately x=5–8H. The $\sigma_{slipstream}$ profile witnesses a gradual increase approaching the tail of the train, and after the tail the gradient becomes significantly steeper, and achieves its maximum at approximately x=4–6H.

According to the slipstream profiles of each model, as presented in Fig. 5, the difference between medium and fine grids with respect to $\overline{U}_{slipstream}$ is minor, while shifting to the coarse grid has a much stronger impact on $\overline{U}_{slipstream}$. Compared with SAS, $\sigma_{slipstream}$ shows a stronger dependence on grid size for both URANS and IDDES. The lower influence of SAS grid size on $\sigma_{slipstream}$ may be due to its scale-adaptive nature, although it is unclear why. The maximum magnitude of $\overline{U}_{slipstream}$ and $\sigma_{slipstream}$, and their corresponding locations, are presented in Table 3. The discrepancy between the wind tunnel and numerical results is explicitly discussed in Section 4; for example, the existence of a local minimum near the tail in experimental data is not captured in any of the numerical simulations.

Table 2
Meshing parameters.

Mesh		Coarse	Medium	Fine
Cell size	Train surface mesh	0.015H–0.12H	0.0075H–0.06H	0.00625H–0.05H
	Under-body refinements	0.015H–0.06H	0.0075H–0.015H	0.00625H–0.0125H
	Wake refinements	0.06H–0.12H	0.015H–0.06H	0.0125H–0.05H
	Far-field refinements	0.24H–0.96H	0.12H–0.48H	0.1H–0.4H
No. of inflation layers		4	8	10
Train surface wall y^+		20–150	10–50	5–30
No. of cells (millions)		3.3	17.4	26.6

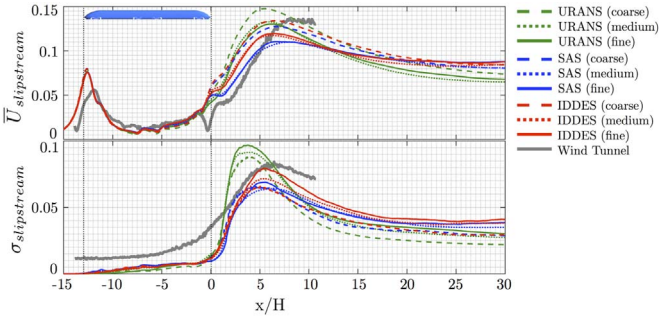

Fig. 5. A comparison of $\overline{U}_{slipstream}$ and $\sigma_{slipstream}$ for the three different turbulence models with results from experiments, showing the effect of grid resolution.

Table 3
The critical values in grid resolution comparison.

Grid resolution	$\overline{U}_{slipstream}$		$\sigma_{slipstream}$	
	Maximum	Location (x/H)	Maximum	Location (x/H)
URANS (coarse)	0.148	5.50	0.088	4.08
URANS (medium)	0.133	5.87	0.092	3.82
URANS (fine)	0.130	6.24	0.097	3.77
SAS (coarse)	0.128	6.82	0.066	4.56
SAS (medium)	0.110	8.13	0.064	6.40
SAS (fine)	0.111	6.61	0.069	5.61
IDDES (coarse)	0.134	6.82	0.066	5.03
IDDES (medium)	0.118	5.98	0.072	5.50
IDDES (fine)	0.120	6.56	0.079	5.61
Wind tunnel	**0.137**	**8.03**	**0.084**	**6.46**

3.1.2. The influence of timestep

The timestep study is based on the fine mesh, maintaining all other solver settings and only varying the timestep. This study examines 3 different timesteps: $\Delta t = 0.05T_{ref}$, $0.025T_{ref}$ and $0.0025T_{ref}$. The smallest timestep of $0.0025T_{ref}$ is chosen because this restricts the Courant number $\leq$1 for the typical smallest cells of the fine grid, which is one of the suggested criteria for conducting DES simulations. The largest timestep of $0.05T_{ref}$ is approximately 1/30 of the period of the dominant wake frequency, which is ideal for URANS simulations, as only the dynamics of dominant flow features are resolved. Additionally, all turbulence models are compared at the timestep of $0.025T_{ref}$ to evaluate the performance of the turbulence models based on an identical medium timestep.

The effect of timestep is illustrated in Fig. 6, and the magnitudes and locations of the maximum $\overline{U}_{slipstream}$ and $\sigma_{slipstream}$ are presented in Table 4. Percentage differences in $\overline{U}_{slipstream}$ for the URANS, SAS and IDDES models are 5%, 15% and 12%, respectively, relative to the wind

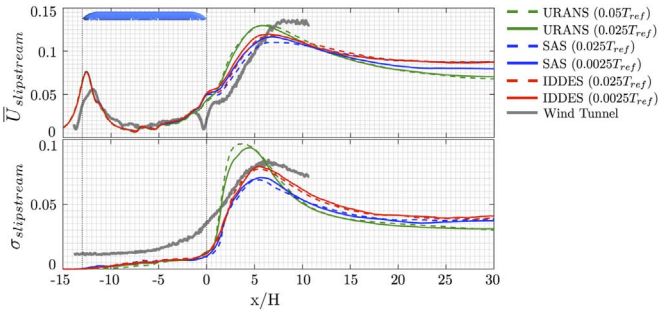

Fig. 6. The comparison of $\overline{U}_{slipstream}$ and $\sigma_{slipstream}$ under timestep effect.

Table 4
The critical values in timestep comparison.

Grid resolution	$\overline{U}_{slipstream}$		$\sigma_{slipstream}$	
	Maximum	Location (x/H)	Maximum	Location (x/H)
URANS ($0.05T_{ref}$)	0.130	6.24	0.097	3.77
URANS ($0.025T_{ref}$)	0.130	5.82	0.094	4.56
SAS ($0.025T_{ref}$)	0.111	6.61	0.069	5.61
SAS ($0.0025T_{ref}$)	0.117	6.82	0.071	5.61
IDDES ($0.025T_{ref}$)	0.119	6.61	0.078	5.61
IDDES ($0.0025T_{ref}$)	0.120	6.56	0.079	5.61
Wind tunnel	**0.137**	**8.03**	**0.084**	**6.46**

tunnel result. For the $\overline{U}_{slipstream}$ prediction, there is a good match before the flow approaches the tail, while further downstream, the differences from the observed experimental variation are higher. This is likely to be connected with the predicted $\sigma_{slipstream}$ variation, as the turbulence level in the wake is much higher than that along the train. For the range of timesteps considered, the accuracy of predicting highly turbulent flow is only weakly dependent on the timestep, except for the URANS model. Additionally, the three cases, URANS ($0.025T_{ref}$), SAS ($0.025T_{ref}$) and IDDES ($0.025T_{ref}$), have the same timestep and are based on the same mesh, allowing a direct comparison between the performance of the turbulence models. The results from Fig. 6 show that the difference between SAS and IDDES is small in terms of $\overline{U}_{slipstream}$, while IDDES has a slightly better prediction of $\sigma_{slipstream}$. URANS over-predicts both $\overline{U}_{slipstream}$ and $\sigma_{slipstream}$, and this is consistent with the difference in mean and transient flow structures presented in Section 3.2.

3.1.3. Aerodynamic drag coefficient

The train aerodynamic drag coefficient (C_D) for each case is listed in Table 5. Overall, this shows that the differences between the C_D predictions are very small for the different cases. For example, the largest difference between the two cases, IDDES-medium-$0.0025T_{ref}$ and URANS-fine-$0.025T_{ref}$, is approximately 4%. One explanation is that due to the unique shape of HSTs, the skin friction is the main source of C_D for typical full-scale trains (Baker, 2010). In this study, despite the reduction of the train length-to-height ratio, skin friction still contributes to a large proportion of the aerodynamic drag. Numerically, the skin friction prediction depends on the train surface boundary layer modelling, while the three models utilise the same RANS approach for wall modelling. These results indicate that compared with slipstream assessment, the prediction of C_D is less dependent on the sophistication of the turbulence modelling, mesh quality and timestep. This suggests that for future studies where C_D is the main interest, a more expensive model would not seem justified.

3.2. Typical case analysis

Based on the preliminary analysis in Section 3.1, a representative case for each model was selected for more detailed analysis, focusing on gust analysis, the time-averaged wake structure and the wake dynamics.

For URANS, the case with timestep=$0.05T_{ref}$ and the coarse mesh was utilised, because Section 3.1 shows that URANS predictions are not sensitive to grid size, at least beyond a minimum level. Whilst there is some timestep dependence, the underlying philosophy for selection here is that the URANS model should be considerably cheaper than the other more complex models, especially as the turbulent time and length scales are not a function of temporal or spatial modelling scales.

The medium mesh with the timestep of $0.025T_{ref}$ was selected for SAS, to optimise the balance between the cost and accuracy. As an adaptive method, its accuracy is based on the solver settings, switching between URANS and LES-like modelling capability as spatial and temporal resolution are increased.

Table 5
The comparison of C_D for all simulation cases.

Grid resolution	$0.05T_{ref}$	$0.025T_{ref}$	$0.0025T_{ref}$
Fine	0.267 (URANS)	0.265 (URANS) 0.269 (SAS) 0.274 (IDDES)	0.268 (SAS) 0.273 (IDDES)
Medium	0.268 (URANS)	0.269 (SAS)	0.276 (IDDES)
Coarse	0.271 (URANS)	0.274 (SAS)	0.274 (IDDES)

For IDDES, the fine mesh with a timestep of $0.0025T_{ref}$ was employed, as good practice for DES simulations requires a local Courant number of unity or less. Overall, IDDES is typically used to study transient flow behaviour, with a range of spatial (and temporal) scales extending into the inertial subrange.

In practice, computational cost is one of the important parameters in determining the selection of a turbulence model. The ratio of the estimated computational costs of the three representative cases are 1:10:20 (URANS:SAS:IDDES). The IDDES simulation used approximately 40 KCPU hours on the Australian *National Computing Infrastructure* (NCI) (RAIJIN) high-performance computing cluster, typically running on 128–256 cores. As better accuracy is typically associated with higher cost, a compromise often needs to be made with turbulence model selection. One of the aims is to quantify the level of accuracy of each turbulence model for predicting different flow aspects, and provide guidelines in selecting the models that satisfy accuracy requirements at minimum cost.

3.2.1. Gust analysis

Based on the TSI guidelines (European Union Agency for Railways, 2014) that define how slipstream should be measured, the time variation of the velocity should be recorded at 3 m distance from the vertical centreplane of the train, recorded with two adjacent probes placed at least 20 m apart. The recording time needs to be sufficiently long to capture the entire flow disturbance including the wake. Furthermore, a 1 second moving average (1s MA) filter is applied to the raw data, and the maximum slipstream value is calculated based on the mean of the filtered peak value plus two standard deviations.

Gust analysis artificially replicates the field measurements of full-scale testing to obtain an ensemble average of the temporal slipstream data as introduced above. This study utilises the *Moving Probe technique*, which was previously applied by Muld et al. (2012b) to study slipstream under TSI regulations.

To begin with, a brief introduction of the gust analysis technique is presented. The first step is to place an artificial probe at the starting point of a slipstream measurement line, and then allow this probe to move downstream at the speed of U_∞. Over the time taken for this probe to travel from the start to the end point, U_{GF} and V_{GF} are recorded, and then $U_{slipstream}$ is calculated based on Eq. (7), and plotted as grey solid curves in Fig. 7. To replicate the 20 m distance between two individual measurements in a field testing environment, the artificial moving probes are released every $5T_{ref}$. Thus, within the total simulation sampling time of $195T_{ref}$, 58 independent measurements can be made (29 at each side), which satisfies the requirement of minimum 20 independent measurements of the TSI regulations (European Union Agency for Railways, 2014). The peak values of individual measurements are plotted as black dot points, and the mean and standard deviation of the peak values are calculated and presented in Table 6. Next, the equivalent of a 1s MA filter is applied to each data set, and presented as light blue curves in Fig. 7, with the peak values indicated by the blue dot points. The final maximum slipstream velocity $\overline{U}_p + 2\sigma_{uv}$ under a 1s MA filter is calculated and presented in Table 6. In practice, the maximum value would be compared with the

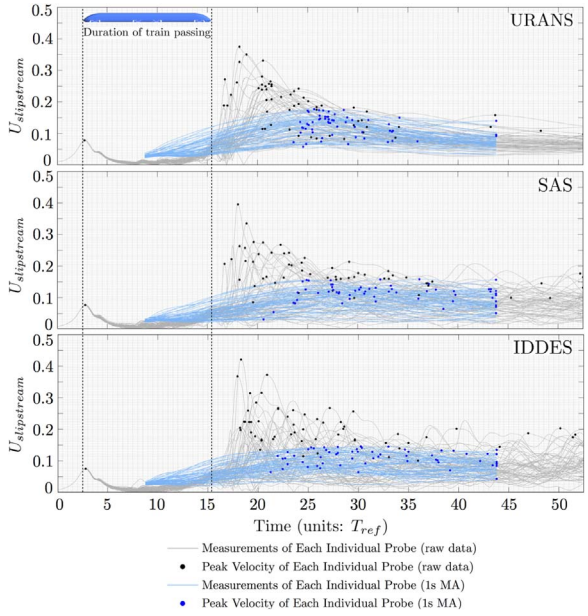

Fig. 7. The gust analysis based on the measurements from the artificial moving probe technique under TSI regulation. (For interpretation of the references to colour in this figure caption, the reader is referred to the web version of this paper.)

Table 6
The unsteady statistics of gust measurement with and without applying a 1 second moving average.

Grid resolution	Without 1s MA			With 1s MA		
	Mean peak ($\overline{U}_p$)	σ_{uv}	$\overline{U}_p + 2\sigma_{uv}$	Mean peak ($\overline{U}_p$)	σ_{uv}	$\overline{U}_p + 2\sigma_{uv}$
URANS	0.189	0.073	0.335	0.125	0.033	0.189
SAS	0.183	0.060	0.302	0.114	0.028	0.170
IDDES	0.207	0.065	0.338	0.111	0.024	0.159
Wind tunnel	**0.322**	**0.138**	**0.597**	**0.118**	**0.021**	**0.159**

maximum allowable slipstream velocity specified by TSI as a part of an acceptance procedure. In this study, the duration of the equivalent sampling time of per artificial probe is $52T_{ref}$, with the starting and ending time for the train passage corresponding to $2.5T_{ref}$ and $15.4T_{ref}$, respectively.

From Fig. 7, the models predict that the maximum $U_{slipstream}$ occurs in the wake about $2–25T_{ref}$ after the tail. Although all the turbulence models depict a statistically similar distribution, a significant run-to-run variance is observed between model data sets, especially for IDDES. The skewness of the time for the raw peak velocities (black dot points) within the wake for URANS, SAS and IDDES is 1.85, 1.15, 1.39 respectively. The percentage differences of the filtered $\overline{U}_p + 2\sigma_{uv}$ values for URANS, SAS and IDDES are +18.9%, +6.9% and +0.0%, respectively, relative to the experimental measurements. This large variation is also reported in full-scale and scaled experiments, and this is indeed one of the practical difficulties in quantifying slipstream (Bell et al., 2015; Baker, 2010). The underlying cause can be seen through examining time-averaged and transient wake properties in Sections 3.2.2 and 3.2.3.

Perhaps of interest is that the maximum peak gust velocity observed in individual runs can be more than a factor of two higher than the filtered $\overline{U}_p + 2\sigma_{uv}$ level, since the pressure disturbance varies with the square of the velocity, this equates to more than a factor of four in the force experienced by a commuter.

3.2.2. Time-averaged wake structure

Based on the results from previous studies, the dominant wake flow structure of a HST is a pair of counter-rotating vortices (Bell et al., 2016a). For this study, the time-averaged wake structure is visualised by x-vorticity (streamwise), in-surface projected velocity vectors and the boundaries of the vorticity-dominated regions, on six vertical planes in the wake, as presented in Fig. 8. As the time-averaged flow structure is symmetric about the mid-plane, only the left half of the flow field is presented. The vorticity is calculated based on the normalised spanwise and transverse velocities. The boundary of the trailing vortex structure corresponds to the iso-line of $\Gamma_2 = 2/\pi$, which is a common vortex identification method often chosen by experimentalists (Graftieaux et al., 2001). The two green asterisks represent the locations of trackside (z=0.05H) and platform (z=0.3H) slipstream measurement height based on TSI specifications (European Union Agency for Railways, 2014).

Through Fig. 8, the downstream evolution of the time-mean trailing vortices can be visualised as the plane shifts from x=0.5H to x=6H. Qualitatively, all three methods show a similar flow structure to that from the wind tunnel measurements. As the vortices move downstream, they roll over the rails and move apart from each other in the spanwise direction. Despite vorticity diffusion and cross-annihilation, the boundary size increases as the vortical structures advect downstream.

Quantitatively, compared with SAS, IDDES and experimental measurements, the vortex boundary predicted by URANS crosses the slipstream measurement lines at an earlier downstream point. As the vortex core contains lower momentum fluid, this induces a higher local slipstream velocity, consistent with the predictions in Figs. 5 and 6. This widening of the wake can also be seen in the planar phase-averaged and instantaneous coloured contours of $U_{slipstream}$ in Section 3.2.3.

From the contribution of large-scale streamwise vortical structures to the overall wake structure, it can be seen that the slipstream velocity is not only sensitive to the strength of the trailing vortex arms, but also their location. Therefore, accurately predicting the location and size of these vortices is critical for accurate slipstream assessment. As the wake structure is highly turbulent and shows strong variation between runs, representative prediction of the vortex location, size and cross-stream movement is challenging both numerically and experimentally. Experimentally, the location of the vortices may be affected by the environment conditions, for example the ambient wind conditions, and invasive measurement techniques. Numerically, to achieve good accuracy of the predicted $U_{slipstream}$ requires adequate resolution of the region for up to at least 5–10H downstream, since this is where the maximum slipstream velocity occurs. This requires a large mesh refinement region in the wake and a sufficiently small timestep, satisfying both requirements can be computationally demanding.

3.2.3. Wake dynamics

According to the wind tunnel experiments, the wake witnesses a strong spanwise oscillation at a Strouhal number (St_W) of 0.19–0.21, based on train width (W) (Bell et al., 2016a). In this study, the spanwise oscillation is visualised by phase-averaging the pressure coefficient C_P in a horizontal plane at z=0.15H. This study adopts the same formula of calculating C_P as used for the wind tunnel experiments (Bell et al., 2016b), which is defined as:

$$C_P = \frac{P_i - P_s}{P_t - P_s}, \tag{8}$$

where P_i is the local static pressure that C_P is based on, and P_t is the total pressure, noting that due to the limitation of the measuring technique, it only takes the streamwise component of velocity into account. P_s is the reference static pressure from an upstream reference pitot-static tube. As for the numerical simulations the reference

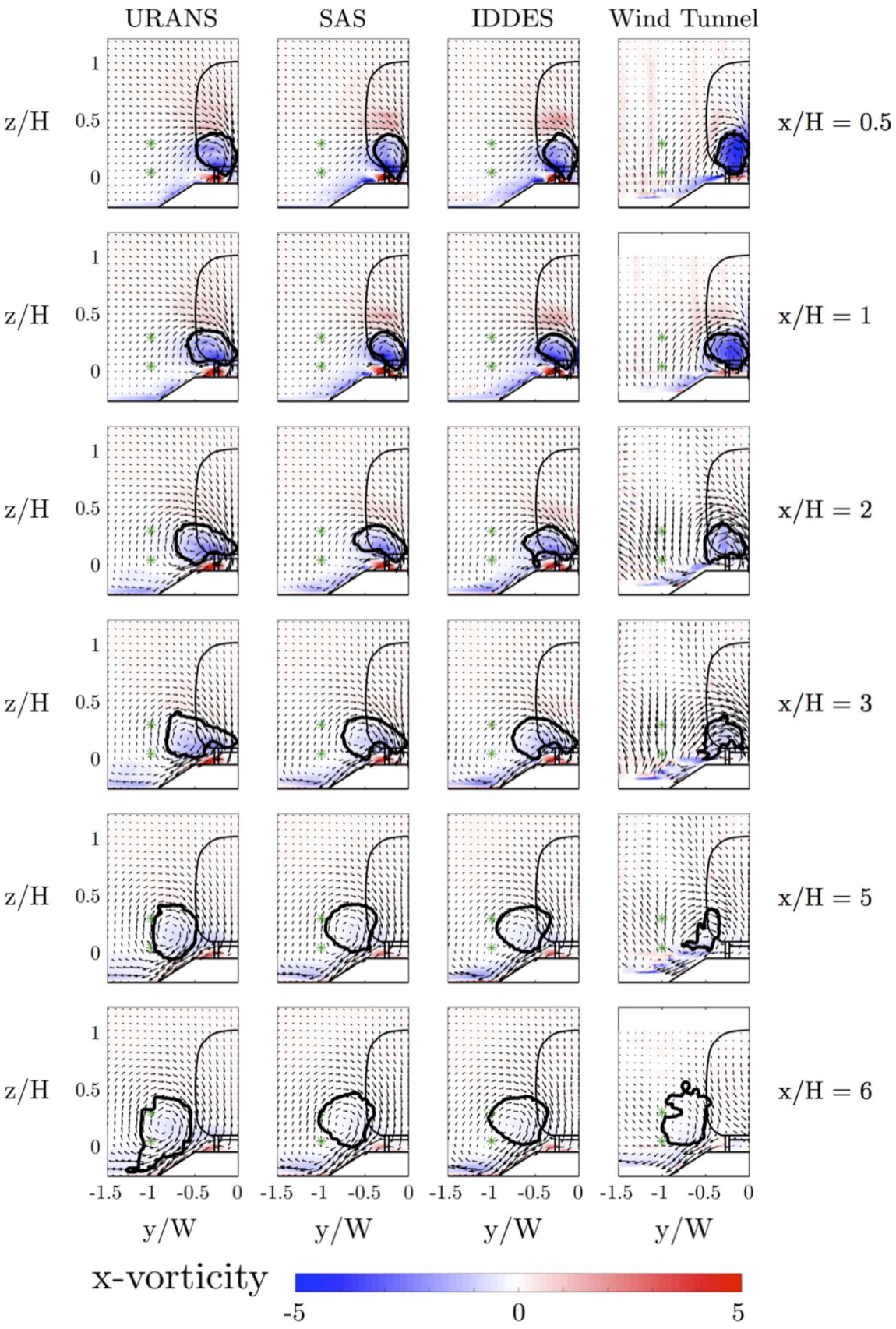

Fig. 8. The comparison of time-averaged wake structure. (For interpretation of the references to color in this figure caption, the reader is referred to the web version of this paper.)

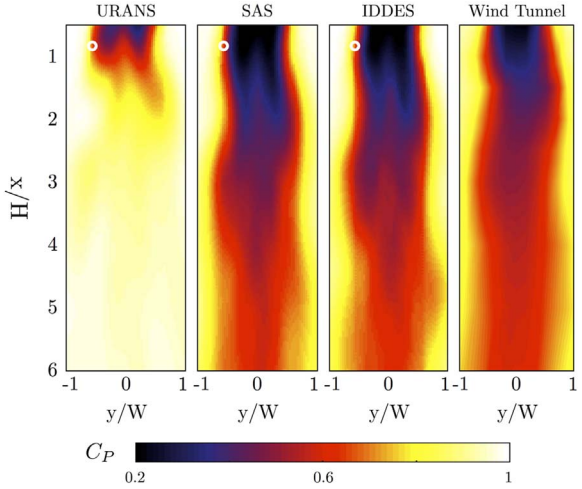

Fig. 9. The comparison of transient wake structures predicted by different turbulence models based on the phase-averaged C_P in a horizontal plane at z=0.15H.

pressure is defined as zero static pressure at outlet, for the numerical comparison a value of $P_s = -0.025$ is used to account for the increased downstream losses in the wind tunnel relative to the open-domain numerical model. The phase-averaging is conducted based on the signal at a reference point with coordinates (0.84H, −0.5W, 0.15H), visualised by the white circles in Fig. 9.

As shown in Fig. 9, the spanwise oscillation observed in the experiments is clearly captured by all three models. Despite the different time and mesh resolutions, SAS and IDDES predict wake structures consistent with the wind tunnel experiments, with the prediction of the URANS model less good. The predicted longitudinal wavelength of the spanwise motion is close to 3H in each case.

Proper Orthogonal Decomposition (POD) is also used to examine the performance of each turbulence model to resolve the detailed makeup of transient wake structures. POD is a widely used technique to extract the coherent flow structures from a turbulent flow field, by calculating the optimal orthogonal bases (modes) of fluctuations. This study employs the snapshot POD method, which was initially proposed by Sirovich (1987), and has been applied to study HST wake structures based on both numerical (Muld et al., 2012a) and experimental data (Bell et al., 2016b). In this study, the POD is conducted based on the total pressure (in line with the experiments) on a vertical plane at the location of x=0.5H. The first four energetic modes are presented in Fig. 10, and the corresponding frequency (St_W) of each mode is determined.

Qualitatively, the first four most energetic modes resolved by different turbulence models are consistent with the wind tunnel measurements (Bell et al., 2016b). The structures of the first two modes show approximately the same sizes of time-averaged longitudinal vortices as depicted in Section 3.2.2. The first mode indicates that the most energetic component is an out-of-phase increase/decrease, which associates with a left/right oscillation in the strength of the trailing vortices, is inline with the phase-averaged results. The spanwise oscillation at $St_W \approx 0.2$ is an indication that the dominant dynamic structure is collaborated with the Karman-like vortex shedding. The second mode shows a simultaneous energy increase/decrease centred on the vortices, corresponding to a longitudinal pulsing of the trailing vortices. The third and fourth modes illustrate smaller energy oscillations above the ballast shoulder. Mode 3 indicates a symmetrical in-phase horizontal/diagonal energy oscillation, while Mode 4 shows an out-of-phase vertical energy oscillation. Modes 1 and 3 acting together can account for the spanwise oscillation of the trailing vortices as they advect downstream. Quantitatively, the mode structures predicted by SAS and DES remain closer to the centreplane, relative to those predicted by URANS. Presumably the loss of centreplane symmetry for modes 3 and 4 is an indication that the length of the dataset used to extract POD modes is insufficient; however, given the computation expense incurred for these simulations, it was difficult to justify increased integration times to better resolve these modes.

In addition to the mode contours illustrated in Fig. 10, the energy percentage of each mode is presented in Table 7 and the cumulative energy percentage distribution of the first 50 modes is shown in Fig. 11. According to Table 7 and Fig. 11, the energy is more concentrated in a few energetic modes for the URANS simulations, whereas IDDES and SAS indicate a wider energy distribution across the modes. For example, the total energy proportion of the first four modes for SAS and IDDES is 0.44 and 0.425 respectively, while for URANS it is 0.726. Additionally, to recover 80% of the total fluctuating energy, URANS, SAS and IDDES require 6, 24 and 32 modes respectively. This is inline with the nature of each turbulence model that URANS only predicts the dominant structures, while IDDES and SAS resolve smaller flow structures and obtain a wider turbulence spectrum, as is discussed further below.

Additionally, the frequency content of each modelled wake is compared based on the power spectral density of U_{TF} at the point (1H, −0.4W, 0.2H). The experimental data shows a wide band at a dominant frequency of St=0.21 (Bell et al., 2016a). Spectral analysis of the velocity signals from numerical simulations at the same point is presented in Fig. 12. In terms of the dominant shedding frequency, all three methods achieve good agreement with the experimental data of St=0.19–0.21, suggesting a Karman-like vortex shedding from the side surfaces of the train, consistent with the left–right oscillation observed in the phase-averaged wake. With respect to the broadness of the frequency spectrum, as expected, URANS has only two narrow peaks, consistent with its failure to capture finer-scale wake structures. Both SAS and IDDES show a slower decay at higher frequencies, implying that a greater range of smaller flow structures is resolved, and this is verified by the turbulent kinetic energy cascade plot presented in Fig. 13.

The turbulent kinetic energy spectra at the same near-wake point (1H, −0.4W, 0.2H) are compared to determine the minimum turbulent length scale that each method can resolve, and to indicate how energy is transferred from larger to smaller length scales. Fig. 13 shows that all three methods achieve a similar prediction to beyond the maximum energy containing scales, which suggests that all the models can reasonably predict the formation of dominant turbulence structures in the near-wake region. In the inertial subrange, both the SAS and IDDES spectra appear consistent than the expected −5/3 ($\simeq -1.67$) theoretical slope (Pope, 2000), even though SAS shows a steeper gradient approaching the dissipation range. Specifically, for the linear part within the inertial subrange, using least-squares linear regression, the gradients within a 95% confidence interval (shown in the brackets) of SAS and IDDES are −2.10(− 2.40 to − 1.81) and −1.78(− 2.01 to − 1.54) respectively. Thus, statistically the IDDES model is consistent with the expected energy falloff in the inertial subrange. In contrast, URANS does not capture the inertial subrange, due to its increased damping. The linear inertial subrange is not clearly identifiable for URANS, but for comparison, its gradient within the same range is approximately −3.53(− 3.76 to − 3.31). Additionally, the prediction of the correct energy transfer to higher wavenumbers implies that smaller turbulence scales are better resolved by IDDES model. However, of course, resolving smaller turbulence scales can be very expensive; for example, the IDDES case is approximately 20 times more expensive than the URANS simulation.

4. Validation and uncertainty analysis

In terms of the slipstream assessment, time-averaged wake structure and wake dynamics, in general good agreement is seen between the different turbulence model predictions and physical experiments. In addition to the relatively small influences of the grid resolution and

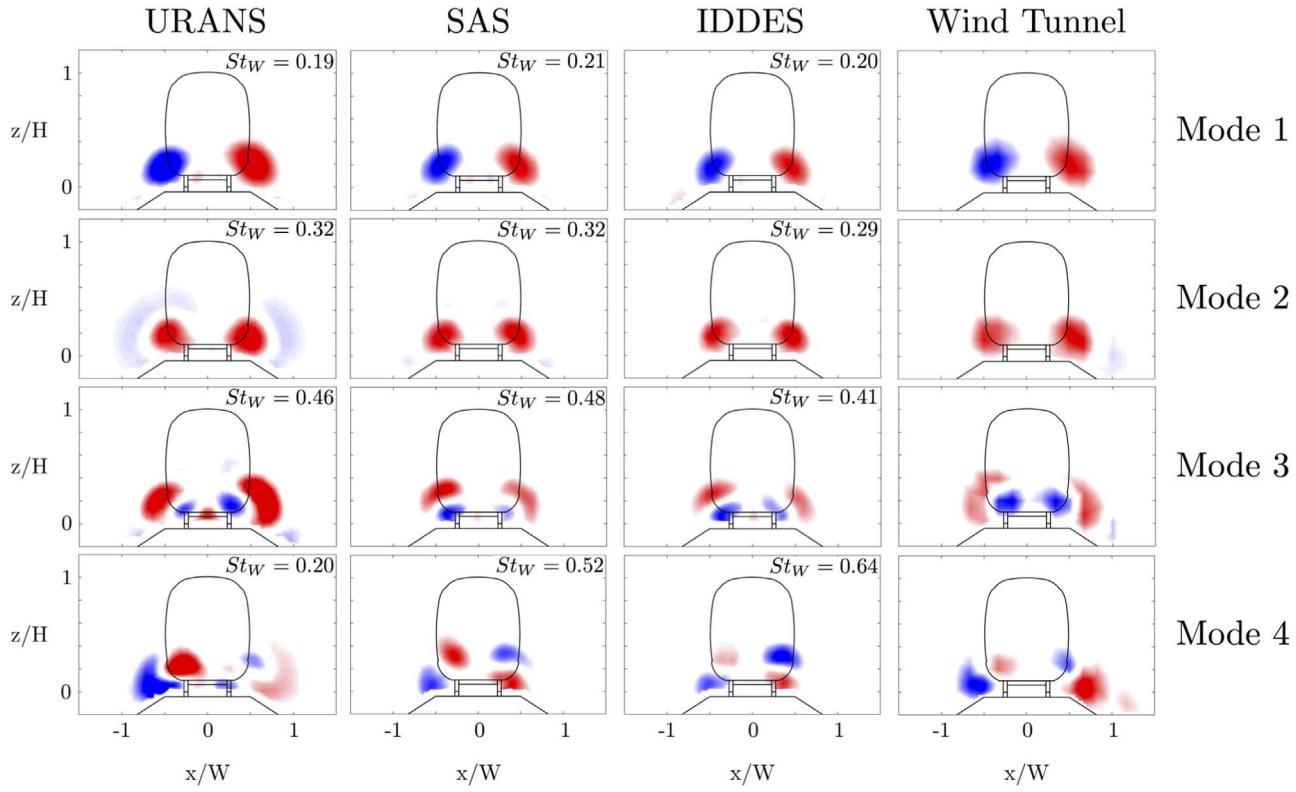

Fig. 10. The comparison of first four POD mode structures at x=1H.

Table 7
Energy percentage of the four most energetic POD modes.

Grid resolution	URANS	SAS	IDDES	**Wind tunnel**
Mode 1	0.499	0.240	0.246	**0.235**
Mode 2	0.120	0.079	0.077	**0.069**
Mode 3	0.072	0.066	0.054	**0.038**
Mode 4	0.047	0.055	0.048	**0.036**
Total	0.726	0.440	0.425	**0.387**

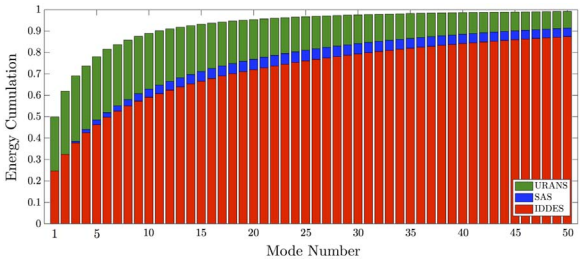

Fig. 11. The cumulative energy percentage with respect to the number of modes.

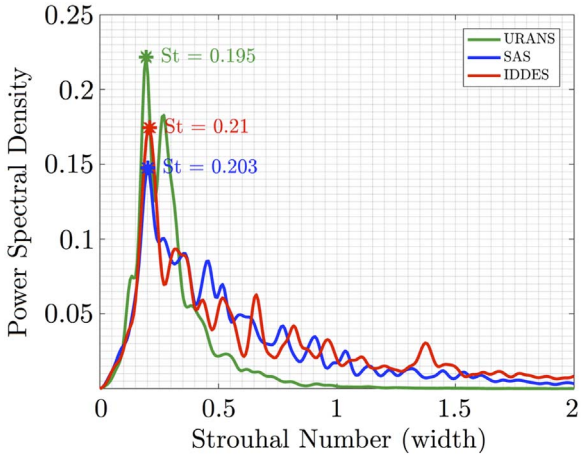

Fig. 12. The comparison of wake shedding frequency based on St_W at the point of [1H, −0.4W, 0.2H].

timesteps, potential causes of discrepancies between the numerical and experimental results in each region are discussed below.

4.1. Nose region

First of all, the discrepancy in the peak slipstream velocity magnitude, as shown in Section 3.1 might be caused by slightly different floor configurations. Even though the cross-sectional dimensions of the ballast for CFD and wind tunnel models are identical, for the numerical simulations the ballast starts at the domain inlet, whereas the ballast for wind tunnel experiment only starts just upstream of the head of the train with a ramp (Bell et al., 2014) (due to restrictions imposed by the working section of the wind tunnel). Additionally, the slight shift of the location of the peak $\overline{U}_{slipstream}$ location might be caused by a slightly different length of the HST models: the wind tunnel model has an exact length of 5 m, while the numerical model has a slightly longer length of 5.165 m based on the model provided by the DIN Standards Railway Committee (FSF, 2014).

4.2. Train side boundary layers

The higher slipstream standard deviation seen along the length of the train is due to upstream turbulence present in the tunnel. In comparison, the numerical simulations show negligible standard deviation along the train, despite the turbulence level at the inlet nominally being approximately set to the tunnel background turbulence level. This suggests that it is necessary to better duplicate upstream background turbulence, including relevant time and length scales of turbulent structures. FLUENT has two different ways to

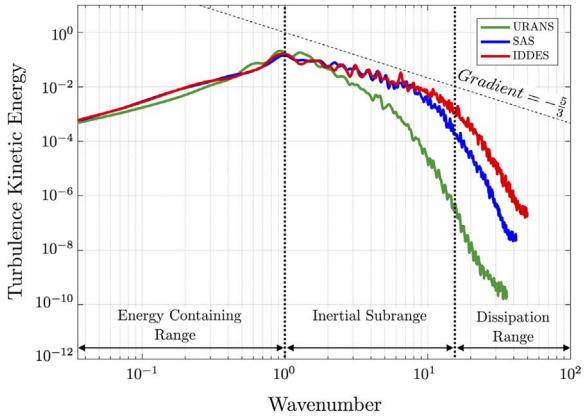

Fig. 13. The turbulence kinetic energy cascade at the point of [1*H*, −0.4*W*, 0.2*H*].

generate synthetic turbulence at the domain inlet. Although not included for the current set of simulations, this is clearly worth exploring for future modelling efforts.

4.3. Near-wake region

The main discrepancy in the near-wake region (around the tail) is that the wind tunnel experiment shows a local slipstream minimum, which is not seen in any of the numerical simulations. Possible causes include the following. First of all, slight simplification of the numerical HST model, especially the underbody structures, may alter the underbody flow which interacts with the downwash over the upper surface in the near-wake region.

Secondly, as this local minimum is not recorded in other moving model experiments and full-scale testing for the same train model, this may imply that the near-wake flow is sensitive to the wind-tunnel measurement techniques (Bell et al., 2014). The slipstream velocity is calculated based on U_{GF} and V_{GF} (Eqs. (6) and (7)). While in most of the wake region U_{GF} is significantly higher than V_{GF}, near the tail the magnitude of U_{GF} drops to zero, and then gradually increases on moving further downstream. Therefore, in the region, $U_{slipstream}$ is dominated by V_{GF}. The experiments use 4-hole cobra probes to determine U_{TF} and V_{TF}. In terms of the raw measuring data, the V_{TF} is much smaller than U_{TF} by an order of magnitude, and this might amplify errors in this region.

4.4. Intermediate-wake region

The discrepancy in the intermediate wake (x=5–8H) may be caused by amplification of upstream deficiencies or local effects. The difference in background turbulence levels between the simulations and experiments may be one possible cause. In addition, the peak slipstream velocity is recorded about 8H behind the tail, which is moving beyond the optimal working section of the tunnel. Imposed pressure gradients in this region may have a small effect on the results.

5. Conclusion

In this study, the ability of three widely used turbulence models to predict the flow past a high-speed train is investigated as a function of grid resolution and timestep. This is achieved through a comparison with wind-tunnel experimental data, based on accuracy in predicting slipstream velocity profiles and correlation with wake structures.

Although simulations based on different turbulence models show qualitatively consistent results with wind tunnel measurements for slipstream assessment, quantitatively the predictions do show a level of dependence on grid resolution and timestep choice. In contrast, all the turbulence models demonstrate a consistency in predicting C_d, which means that if the drag evaluation is the sole purpose, utilisation of IDDES or even SAS is not justified. At least, for the simplified model we have considered.

Naturally, HST slipstream assessment depends strongly on flow development around the train and downstream. Qualitatively, the dominant time-averaged and transient flow features, longitudinal vortices and corresponding spanwise oscillation can be predicted by all three models. Quantitatively, URANS fails to predict the cross-stream development of the trailing vortices and the correlated dynamic response, which makes it unsuitable for quantitative slipstream assessment. IDDES shows superior consistency with the experimental data, perhaps due to its ability to capture a wider range of turbulence scales in the wake. As the first systematic study of using SAS to predict the HST slipstream, the results show that SAS may be a reasonable alternative of IDDES as it achieves a similar level of accuracy at a lower cost.

In practice, trade-offs exist between accuracy and computational cost. This paper has attempted to quantify how well each turbulence-model/mesh/timestep combination reproduces different aspects of the flow past a high-speed train, especially in relation to slipstream characteristics and wake dynamics.

References

Baker, C., 2010. The flow around high speed trains. J. Wind Eng. Ind. Aerodyn. 98 (6), 277–298.
Bell, J.R., Burton, D., Thompson, M.C., Herbst, A.H., Sheridan, J., 2014. Wind tunnel analysis of the slipstream and wake of a high-speed train. J. Wind Eng. Ind. Aerodyn. 134, 122–138.
Bell, J.R., Burton, D., Thompson, M.C., Herbst, A.H., Sheridan, J., 2015. Moving model analysis of the slipstream and wake of a high-speed train. J. Wind Eng. Ind. Aerodyn. 136, 127–137.
Bell, J.R., Burton, D., Thompson, M.C., Herbst, A.H., Sheridan, J., 2016a. Flow topology and unsteady features of the wake of a generic high-speed train. J. Fluids Struct. 61, 168–183.
Bell, J.R., Burton, D., Thompson, M.C., Herbst, A.H., Sheridan, J., 2016b. Dynamics of trailing vortices in the wake of a generic high-speed train. J. Fluids Struct. 65, 238–256.
Egorov, Y., Menter, F., Lechner, R., Cokljat, D., 2010. The scale-adaptive simulation method for unsteady turbulent flow predictions. Part 2: application to complex flows. Flow Turbul. Combust. 85 (1), 139–165.
European Union Agency for Railways, 2014. Commission Regulation (EU) No 1302/2014 concerning a technical specification for interoperability relating to the 'rolling stock — locomotives and passenger rolling stock' subsystem of the rail system.
Fossi, A., DeChamplain, A., Akih-Kumgeh, B., 2015. Unsteady rans and scale adaptive simulations of a turbulent spray flame in a swirled-stabilized gas turbine model combustor using tabulated chemistry. Int. J. Numer. Methods Heat. Fluid Flow 25 (5), 1064–1088.
DIN Standards Committee Railway/Normenausschuss Fahrweg und Schienenfahrzeuge (FSF), 2014 ⟨http://www.fsf.din.de⟩.
Graftieaux, L., Michard, M., Grosjean, N., 2001. Combining PIV, POD and vortex identification algorithms for the study of unsteady turbulent swirling flows. Meas. Sci. Technol. 12 (9), 1422.
Hemida, H., Baker, C., Gao, G., 2014. The calculation of train slipstreams using large-eddy simulation. Proc. Inst. Mech. Eng. Part F: J. Rail Rapid Transit 228 (1), 25–36. http://dx.doi.org/10.1177/0954409712460982.
Huang, S., Hemida, H., Yang, M., 2016. Numerical calculation of the slipstream generated by a crh2 high-speed train. Proc. Inst. Mech. Eng. Part F: J. Rail Rapid Transit 230 (1), 103–116.
Menter, F.R., 2012. Best practice: Scale-resolving simulations in ANSYS CFD. ANSYS Germany GmbH, ANSYS Germany, 1–70.
Menter, F., Egorov, Y., 2010. The scale-adaptive simulation method for unsteady turbulent flow predictions. Part 1: theory and model description. Flow Turbul. Combust. 85 (1), 113–138.
Morden, J.A., Hemida, H., Baker, C.J., 2015. Comparison of rans and detached eddy simulation results to wind-tunnel data for the surface pressures upon a class 43 high-speed train. J. Fluids Eng. 137 (4), 041108.
Muld, T.W., Efraimsson, G., Henningson, D.S., 2012a. Flow structures around a high-speed train extracted using proper orthogonal decomposition and dynamic mode decomposition. Comput. Fluids 57, 87–97.
Muld, T.W., Efraimsson, G., Henningson, D.S., 2012b. Mode decomposition and slipstream velocities in the wake of two high-speed trains. Int. J. Railw. Technol.
Östh, J., Kaiser, E., Krajnović, S., Noack, B.R., 2015. Cluster-based reduced-order modelling of the flow in the wake of a high speed train. J. Wind Eng. Ind. Aerodyn. 145, 327–338.
Paradot, N., Talotte, C., Garem, H., Delville, J., Bonnet, J.-P., 2002. A comparison of the numerical simulation and experimental investigation of the flow around a high speed train. In: ASME 2002 Joint US-European Fluids Engineering Division Conference,

pp. 1055–1060.
Pope, S.B., 2000. Turbulent Flows. Cambridge University Press, Cambridge, UK, September, p. 806, ISBN 0521591252.
Railway Applications – Aerodynamics Part 4: Requirements and test procedures for aerodynamics on open track, CEN EN 14067-4, 2013.
Rotta, J.C., 1972. Turbulente Strömungen.
Schulte-Werning, B., Heine, C., Matschke, G., 2003. Unsteady wake flow characteristics of high-speed trains. Proc. Appl. Math. Mech. 2 (1), 332–333.
Sirovich, L., 1987. Turbulence and the dynamics of coherent structures. Part i: coherent structures. Q. Appl. Math. 45 (3), 561–571.
Spalart, P.R., 2009. Detached-eddy simulation. Annu. Rev. Fluid Mech. 41, 181–202.
Yang, Z., Gu, Z., Tu, J., Dong, G., Wang, Y., 2014. Numerical analysis and passive control of a car side window buffeting noise based on scale-adaptive simulation. Appl. Acoust. 79, 23–34.
Zhang, J., Li, J.-j., Tian, H.-q., Gao, G.-j., Sheridan, J., 2016. Impact of ground and wheel boundary conditions on numerical simulation of the high-speed train aerodynamic performance. J. Fluids Struct. 61, 249–261.